SCIENCE ROBOTICS | RESEARCH ARTICLE

BIOMIMETICS

A twist of the tail in turning maneuvers of bird-inspireddrones

Hoang-Vu Phan* and Dario Floreano*

A banked turn is a common flight maneuver observed in birds and aircraft. To initiate the turn, whereas traditional aircraft rely on the wing ailerons, most birds use a variety of asymmetric wing-morphing control techniques to roll their bodies and thus redirect the lift vector to the direction of the turn. Nevertheless, when searching for prey, soaring raptors execute steady banked turns without exhibiting observable wing movements apart from the tail twisting around the body axis. Although tail twisting can compensate for adverse yaw, functioning similarly to the vertical tail in aircraft, how raptors use only tail twisting to perform banked turns is still not well understood. Here, we developed and used a raptor-inspired feathered drone to find that the proximity of the tail to the wings causes asymmetric wing-induced flows over the twisted tail and thus lift asymmetry, resulting in both roll and yaw moments sufficient to coordinate banked turns. Moreover, twisting the tail induces a nose-up pitch moment that increases the angle of attack of the wings, thereby generating more lift to compensate for losses caused by the banking motion. Flight experiments confirm the effectiveness of tail twist to control not only low-speed steady banked turns but also high-speed sharp turns by means of coordinated tail twist and pitch with asymmetric wing shape morphing. These findings contribute to the understanding of avian flight behaviors that are difficult to study in controlled laboratory settings and provide effective control strategies for agile drones with morphing aerial surfaces.

INTRODUCTION

Birds can adapt morphology and kinematics of their wings and tail to diverse flight modes and atmospheric conditions (*1*–*5*). These capabilities have spurred growing interest in replicating morphing mechanisms in winged drones of similar scale (*6*–*8*). Numerous morphing-wing drones have been developed that exhibit improved flight stability (*9*, *10*), higher maneuverability and agility (*11*–*15*), and better energetic efficiency (*13*, *16*) than conventional fixed-wing drones. Despite aerodynamic benefits and shape adaptability, most existing drones display simple morphing capabilities constrained by few mechanical components and degrees of freedom. This means that existing morphing drones lack the level of morphological complexity required to replicate the compatible aerodynamic and inertial characteristics of birds (*5*). In addition, they use a conventional aircraft tail design with both horizontal and vertical surfaces, unlike a bird tail, which has only a morphing horizontal surface capable of twisting around the body axis.

Soaring raptors, including eagles, hawks, and falcons, are frequently observed twisting their tails during banked turns (*3*, *17*), which are common flight maneuvers. In the entry phase of a banked turn, birds twist their tails in the opposite direction to the bank and in the exit phase reverse the tail rotation (*3*, *18*). It is well known that birds twist their tails during turns to compensate for adverse yaw generated by asymmetric drag on the wings (*1*, *3*, *17*, *19*, *20*). However, the mechanism that initiates the roll moment to bank the bird's body is still not well understood. Theoretical studies that model bird tails as delta wings predicted that twisting the tail around the body axis at high angles of attack induces asymmetric leading-edge vortices because of sideslip and, consequently, generates both roll and yaw moments sufficient to initiate a banked turn (*21*–*23*). However, these studies assumed uniform flow and vortices that remained attached to the wing upper surface even at high angles of attack; furthermore, these models did not consider potential airflow disruptions over the tail generated by the proximity of the bird's wings and body (*23*–*25*). Wind tunnel experiments with simplified fixed-wing models (*20*, *26*) reported the generation of roll moment by tail twisting, but the magnitude was too small for effective roll control in birds (*1*, *7*). Understanding the aerodynamic function of tail twist in avian turning maneuvers thereby necessitates consideration of the full flight envelope, but obtaining such flight behavior with birds in controlled laboratory settings is nontrivial.

Here, we studied avian turning maneuvers by means of a raptor-inspired feathered drone with morphing wings and tail. We designed the drone using a bioinformed design approach, considering not only similar structure, geometry, and morphology of a hawk but also its inertial and aerodynamic parameters. We then used the drone to characterize aerodynamic effects induced by tail twisting in banked turns and to validate the results with flight experiments in controlled conditions. We found that the proximity of the tail to the wings, which is typical of raptors, causes asymmetric wing-induced flows over the twisted tail that produce both roll and yaw moments required to initiate, coordinate, and terminate banked turns. In addition, we found that such effects induce a nose-up pitch motion that increases the wing angle of attack and generates additional lift to compensate for lift loss due to the turn. This helps to preserve flight altitude during a steady banked turn without the need for birds to pitch their tails or for aircraft to activate the elevator. Furthermore, we used the drone to validate our hypothesis that birds can use tail twisting also to control high-speed sharp turns and that, in such conditions, a coordination of tail motion with asymmetric wing morphing results in even faster level-flight recovery at the end of agile turning maneuvers.

RESULTS

Raptor-inspired feathered drone

We developed a raptor-inspired drone, named LisRaptor, featuring morphing wings and tail covered by feather-like structures (Fig. 1,

---

School of Engineering, École Polytechnique Fédérale de Lausanne (EPFL), Lausanne, 1015, Switzerland.
*Corresponding author. Email: vu.phan@epfl.ch (H.-V.P.); dario.floreano@epfl.ch (D.F.)

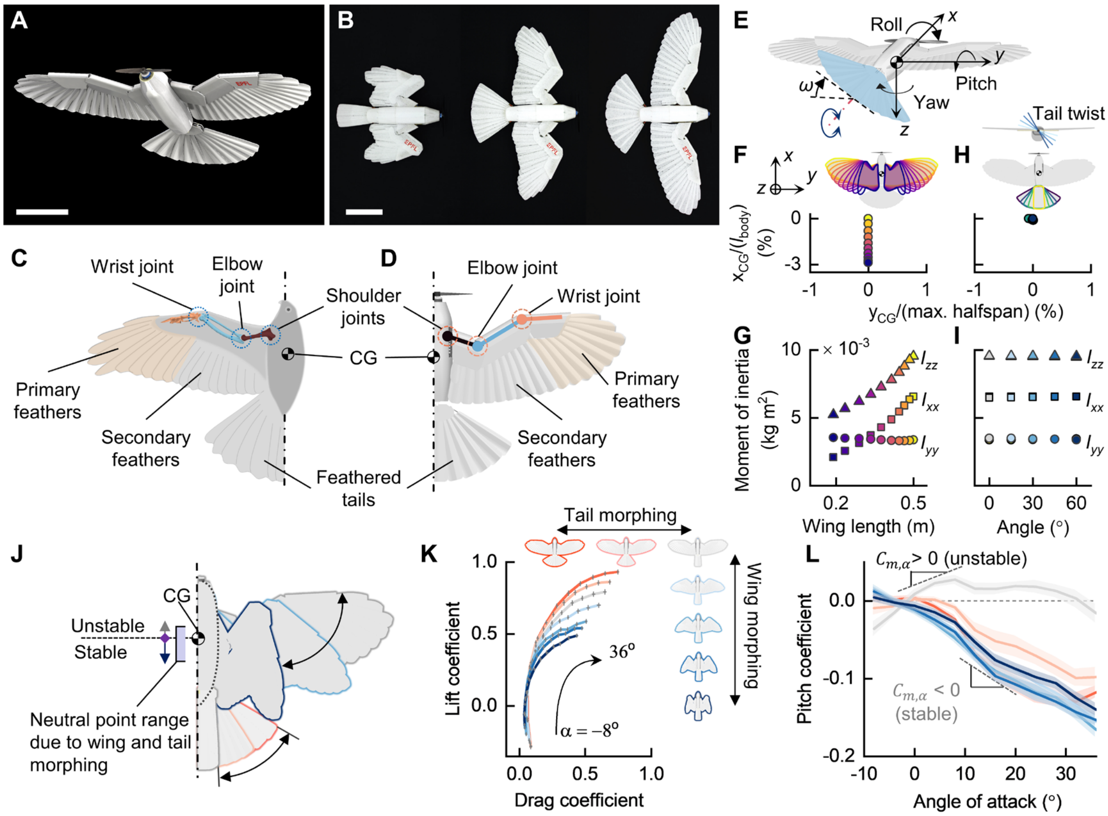

Fig. 1. Bioinformed design and characteristics of the feathered morphing LisRaptor drone. (**A**) LisRaptor with avian-inspired morphing wings and tail. (**B**) Shape morphing allows the drone to change the spans and surface areas of the wings and tail. Scale bars, 20 cm. (**C** and **D**) Coupled motion of bird wing skeletons around elbow and wrist joints (C) inspired the design of the robotic wing skeleton (D). (**E**) Bird-inspired rudderless tail capable of twisting around the body axis. (**F** and **G**) Wing shape morphing minimally alters the location of the CG (F) but strongly affects the roll and yaw moments of inertia, I_{xx} and I_{zz}, respectively, (G) similar to those in birds. (**H** and **I**) The location of the CG (H) and moments of inertia (I) are quite constant with the tail shape morphing and twist. (**J**) Wing and tail shape morphing controls longitudinal stability by altering location of the neutral point. (**K** and **L**) Lift and drag (K) and pitching moment (L) generated by wing and tail shape morphing. Solid lines and gray error bars in (K) [or shaded areas in (L)] indicate the mean value and SD, respectively, obtained from 2400 data points at each measured angle of attack.

fig. S1, table S1, and Materials and Methods). The wing skeleton consists of three segmented linkages replicating the bird's humerus, ulna, and manus that respectively rotate around the shoulder, elbow, and wrist joints with dimensions and mass similar to those of raptor wings (Fig. 1, C and D) (*5*, *27*, *28*). Birds can couple their elbow and wrist motion to change the shape and area of the wing (*29*, *30*). We also coupled the motion of the shoulder, elbow, and wrist joints by a single tendon-driven actuator (Materials and Methods). Bird wings and tail are fully covered by lightweight overlapping feathers (*31*), which we approximated by means of folding foam structures that allow the drone to reduce wing length, wing surface, and tail surface by approximately 60, 53, and 68%, respectively, when fully folded (Fig. 1B and fig. S1).

In contrast with a fixed-wing aircraft's tail, which is used solely for stability and control and is positioned sufficiently away from the wings to minimize negative effects of wing-induced wakes (*32*), avian tails are located comparatively closer to the wing trailing edges, and they play important aerodynamic functions, such as lift augmentation (*33*, *34*), drag reduction (*34*–*36*), and pitch control (*37*). In addition, birds compensate for the absence of vertical tail stabilizers found in aircraft by twisting their tails around the body axis (*17*, *19*, *20*, *38*, *39*). Similar to birds, the morphing tail used here is located close to the drone wings, does not have a vertical rudder, can independently twist around the body axis (Fig. 1E), and can also change pitch angle for longitudinal control (Materials and Methods) (*2*, *7*, *13*). Because the sizes and shapes of tails vary substantially across bird species (*40*), we designed the tail used in this study with a length and shape similar to those of soaring hawks of comparable scales (*41*).

In birds, sweep morphing of aerial surfaces alters not only aerodynamic but also inertial characteristics, two quantities that substantially affect flight maneuverability (*5*). Similarly to raptors during gliding with fully extended wings, the LisRaptor's center of gravity (CG) lies behind the wing aerodynamic center, which is located approximately at the quarter of the wing mean chord (*5*, *42*). When morphing, the CG shifted only by 3% of the full body length (Fig. 1F), similarly to birds (*5*). However, wing extension increased roll and yaw moments of inertia by up to 3-fold and 1.8-fold, respectively (Fig. 1G), consistent with observations of Cooper's hawks and peregrine falcons (*5*) during the elbow and wrist extension (approximately fourfold and twofold, respectively). Tail sweep morphing and twisting did not substantially affect moments of inertia because of the comparatively low mass of the tail, which represents less than 3% of the body mass (Fig. 1, H and I).

We then investigated the static aerodynamic performance of the LisRaptor drone via wind tunnel experiments (Fig. 1, J to L, and fig. S2). Wing morphing altered lift and drag generation and affected pitch stability (Fig. 1, J to L), similarly to birds (*5*). By fully extending the wings with a fully folded tail, the neutral point lied ahead of the CG, causing the drone to be slightly unstable ($C_{m,\alpha} = \partial C_m / \partial \alpha > 0$, where C_m is the pitch coefficient and α is the angle of attack). Folding the wings shifted the neutral point aft of the CG, thus shifting the drone to a stable longitudinal mode ($C_{m,\alpha} < 0$) but decreased lift. In addition, we found that spreading the tail also enabled the drone with fully extended wings to transition from an unstable to stable state while increasing lift (Fig. 1, K and L). These results suggest that birds may prefer to use tail spread morphing rather than wing sweep morphing to control longitudinal stability when flying at low speeds where lift is a priority. The dynamics of the drone should also be evaluated for a full stability analysis, especially for flight in gusty conditions. However, this requires solving numerous complex equations of motion arising from variable morphology body that goes beyond the focus of this study while offering a less intuitive understanding of how stability is maintained compared with static stability analysis (*42*). In summary, these results indicate that the avian-inspired LisRaptor drone displays inertial and aerodynamic properties similar to those of birds and represents a suitable model for studying avian turning maneuvers.

Tail twist controls steady banked turns

We started investigating the role of tail twist in banked turns by conducting aerodynamic characterization in an open wind tunnel (Fig. 2). We found that tail twist contributed to all six axis forces (lift, drag, and side force) and moments (pitch, roll, and yaw moments) of the LisRaptor. Twisting the tail around the body axis (regardless of the rotation direction) reduced its longitudinal surface, thus reducing lift (Fig. 2A). The reduced tail lift caused the drone to experience a nose-up orientation and shift from longitudinally stable to unstable mode (Fig. 2B). During a banked turn, a traditional aircraft rolls around its body axis to redirect the lift vector into the direction of the roll that adds horizontal component providing centripetal acceleration to execute the turn but decreases the vertical lift component and thus flight altitude. To gain more lift, most aircraft deflect the elevator at the tail to generate a pitch-up moment, which increases the wing angle of attack (*14*). Thus, the nose-up orientation induced by the tail twist of the avian-inspired drone may serve a similar role by increasing the overall lift force during the turn.

Twisting the tail tilted the tail lift vector and therefore generated side forces, resulting in yaw moments; namely, a negative tail twist (counterclockwise rotation in Fig. 2C) produced a positive yaw moment (nose yaws to the right) and vice versa (Fig. 2C). We also found that tail twist generated roll moments; namely, negative twist resulted in a positive roll moment (right wing downward) and vice versa (Fig. 2D), consistent with observations of birds (*3*, *18*). Together, these data show that tail twisting enables the roll control required to initiate the banked turn and generates yaw moment that counters the adverse yaw induced by the higher drag of the outer wing during turning. However, when the wings were removed, twisting the tail generated roll moments in the same direction of the

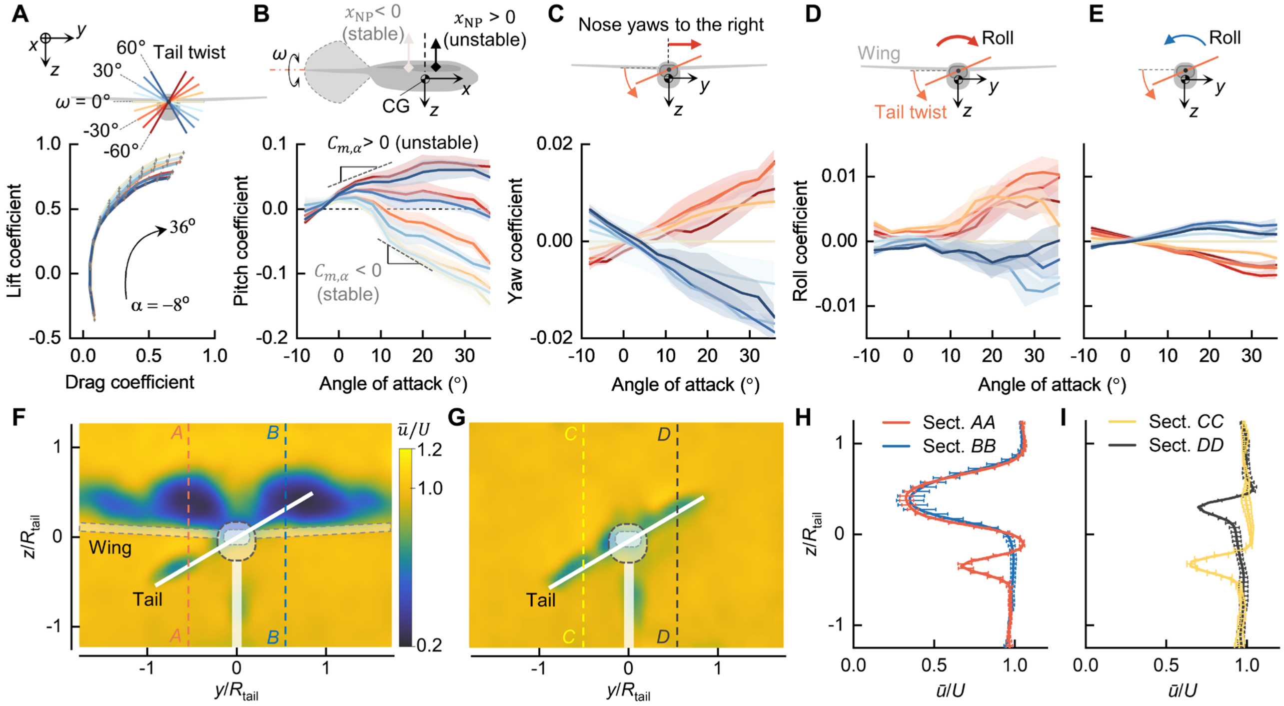

Fig. 2. Aerodynamic characteristics of the LisRaptor with tail twist. (**A**) Twisting the tail reduces the longitudinal surface area, thus reducing lift. (**B**) Pitching moment generated as a result of tail twist. Reduced lift from the tail shifts the drone from stable to unstable configurations by generating more pitch-up moment. (**C**) Tail twist generates a proverse yaw moment that supports the turn. (**D** and **E**) Roll moments in the presence (D) and absence (E) of the wings. (**F** to **I**) Twisting the tail sends the upper tail part into the turbulent wake of the wing. [(F) and (G)] Velocity maps at 50% chord of the tail in the presence (F) and absence (G) of the wings. [(H) and (I)] Velocity profiles at $y = 0.5\ R_{tail} = 0.11$ m ($n = 3$) with the presence of the wings shown in (F) at the sections *AA* and *BB* (H) and the absence of the wings shown in (G) at the sections *CC* and *DD* (I). The measurement was conducted at an inflow velocity of $U_{ref} = 7$ m/s with an angle of attack of $\alpha = 16°$. In (A) to (E), solid lines and shaded areas [gray error bars in (A)] indicate the mean value and SD, respectively, obtained from 2400 data points at each measured angle of attack.

tail motion (Fig. 2E). To gain insight into how wings affect the roll moment generated by the tail, we conducted flow visualization experiments (Fig. 2, F to I). We found that, when twisted, the upper side of the tail entered the low-speed wake region induced by the wings, thereby reducing its force generation (Fig. 2, F and H); in contrast, the other side of the tail, which descended away from the wing, was not affected by the wing-induced wake. Consequently, asymmetric lift between the two sides of the tail generated a roll moment. On the other hand, without the wing ahead, there was no substantial difference in the flow fields between the two sides of the tail (Fig. 2, G and I). Given that the CG location was lower than the pivot point of the tail (rotation axis) (Fig. 2E), twisting the tail increased the moment arm to the upper half and reduced that in the lower half of the tail. As a result, roll moment was generated in the same direction of the tail twist. We confirmed that this roll moment was negligible when the CG was located at the tail rotation axis (fig. S3). Although body-tail interaction occurring near the body centerline may alter aerodynamic force generation (*34*), our results showed that it did not have a substantial effect on rolling moment (fig. S3B).

To test whether the moments generated by tail twist are sufficient to initiate banked turns, we conducted indoor flight experiments (Fig. 3, figs. S4 and S5, and movies S1 to S3). We replicated the banked turn strategy observed in birds by a two-phase tail twist (Fig. 3, A and B) (*18*). The results showed that the LisRaptor could perform banked turns with a turning radius (= 1 per curvature) of 10.8 ± 3.0 m at a bank angle of 31.2° ± 8.5° (Fig. 3, D to L) with roll and yaw motions (Fig. 3, G and I) and nose-up pitch (Fig. 3H) induced by tail twisting (Fig. 3B). To complete the turn, the drone temporarily reversed its tail twist and returned to level flight; if no action was taken, then the drone kept increasing its roll and yaw while decreasing pitch (Fig. 3, G to L), and, as a result, the drone tumbled (movie S3). We also found that the reaction force induced by the tail twist acceleration did not induce a rotation of the drone in the opposite direction (fig. S6). These results suggest that birds may stabilize the exit phase of banked turns by temporarily reversing the tail twist direction instead of relying only on inherent lateral stability (*3*).

Tail twist controls high-speed sharp turns

Flying at high speed through cluttered environments requires sharp turns to avoid obstacles, but the role of tail twist in such turning maneuvers is still unexplored. Although birds can resort to either flapping or gliding maneuverings in a turn (*43*), flapping in birds flying at low speed (*44*–*46*) expends much more metabolic energy than gliding maneuvering does (*47*, *48*). However, whether and how birds execute high-speed sharp turns by gliding maneuvering remain unclear. Because the turning radius is proportional to the square of the flight speed (*4*, *14*), performing a high-speed turn with a small turning radius may require quick deceleration before the turn. Many large birds engaged in agile maneuvers, such as perching (*49*) and recovery from high-speed dive (*50*, *51*), decelerate by executing a rapid pitch-up maneuver to transfer kinetic energy to

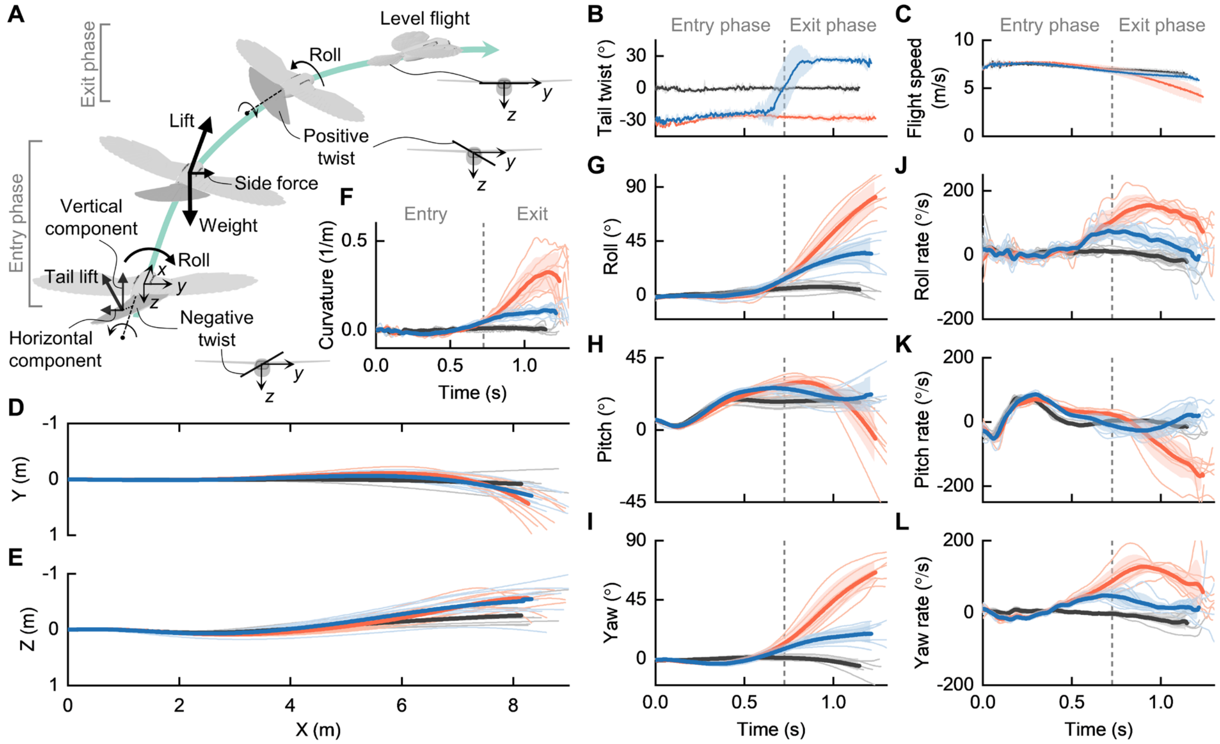

Fig. 3. Flight experiments confirm that drones and birds can merely twist their tails to execute steady banked turns. (**A**) Two-phase turning maneuvers. Negative tail twist initiates a right turn and reverses to positive twist to exit the turn. (**B**) Tail-twist angles in three flight patterns: trimmed flight ($n = 7$, black) and banked turns without ($n = 8$, red) and with ($n = 8$, blue) reversal of the tail twist at the end of the turn. Tail-twist angle is set to be ± 30°, which generates maximum rolling moments. (**C**) Flight speeds during turning. (**D** and **E**) Flight trajectories in the *XY* plane (D) and the *XZ* plane (E). (**F**) Curvature of the turns. (**G** to **I**) Body attitude angles: roll (G), pitch (H), and yaw (I). (**J** to **L**) Body rates: roll rate (J), pitch rate (K), and yaw rate (L). In (B) to (L), thin lines represent individual flight trials; thick lines and shaded areas are the mean and SD from the mean, respectively.

potential energy. Here, we hypothesize that birds may leverage a similar strategy and coordinate tail pitching and twisting to perform sharp maneuvers when flying at high speeds.

We conducted flight experiments on high-speed sharp turning by applying a coordination of rapid pitch-up maneuver and tail twist (Fig. 4). To initiate the pitch-up maneuver, the tail was deflected upward (*23*, *49*, *52*), causing the LisRaptor drone to climb (Fig. 4, A and E). During the climb, negative tail twist was applied to induce roll and yaw movements to the right. When the climbing phase reached peak altitude, the drone reversed the tail twist to exit the turn. We found that the coordination allowed the LisRaptor to perform sharp 90° turns with small turning radii. Experimental results showed that the LisRaptor flying at an initial speed of 8.8 ± 0.5 m/s could turn with a radius of 1.9 ± 0.3 m and a bank angle of 84.4° ± 5.2° [Fig. 4, B to M (black), and movie S4]. The pitch-up response allowed the drone to reduce its speed to 2.9 ± 0.3 m/s at peak altitude (Fig. 4C), thus converting 24.2 ± 2.7% kinetic energy into potential energy while dissipating 64.7 ± 2.3% through aerodynamic braking (Fig. 4G). Nevertheless, tail twist alone could slowly recover the roll motion to level flight in the exit phase of the turn (Fig. 4, H and K, black). To address this issue, we added asymmetric wing folding observed in turning birds (Fig. 4A and fig. S7) (*3*, *18*) and obtained a faster level flight recovery after the turn (Fig. 4, H and K, and movie S5). However, the faster recovery came at a cost of increased turning radius of 3.2 ± 0.6 m. By adjusting the starting time of the asymmetric wing folding during the exit phase, it is possible to regulate the turning radius and heading direction (fig. S8). However, the LisRaptor could not turn with asymmetric wing folding without tail twisting because of adverse yaw effect (fig. S9 and movie S6). These results indicate that tail twisting could play a major role also in sharp turning maneuvers at high flight speeds.

DISCUSSION

These results suggest that tail twisting can play a substantial role in turning maneuvers at both low and high speeds. When twisted, the tail enters asymmetric flow regions induced by the wings, resulting in the generation of both roll and yaw moments that initiate,

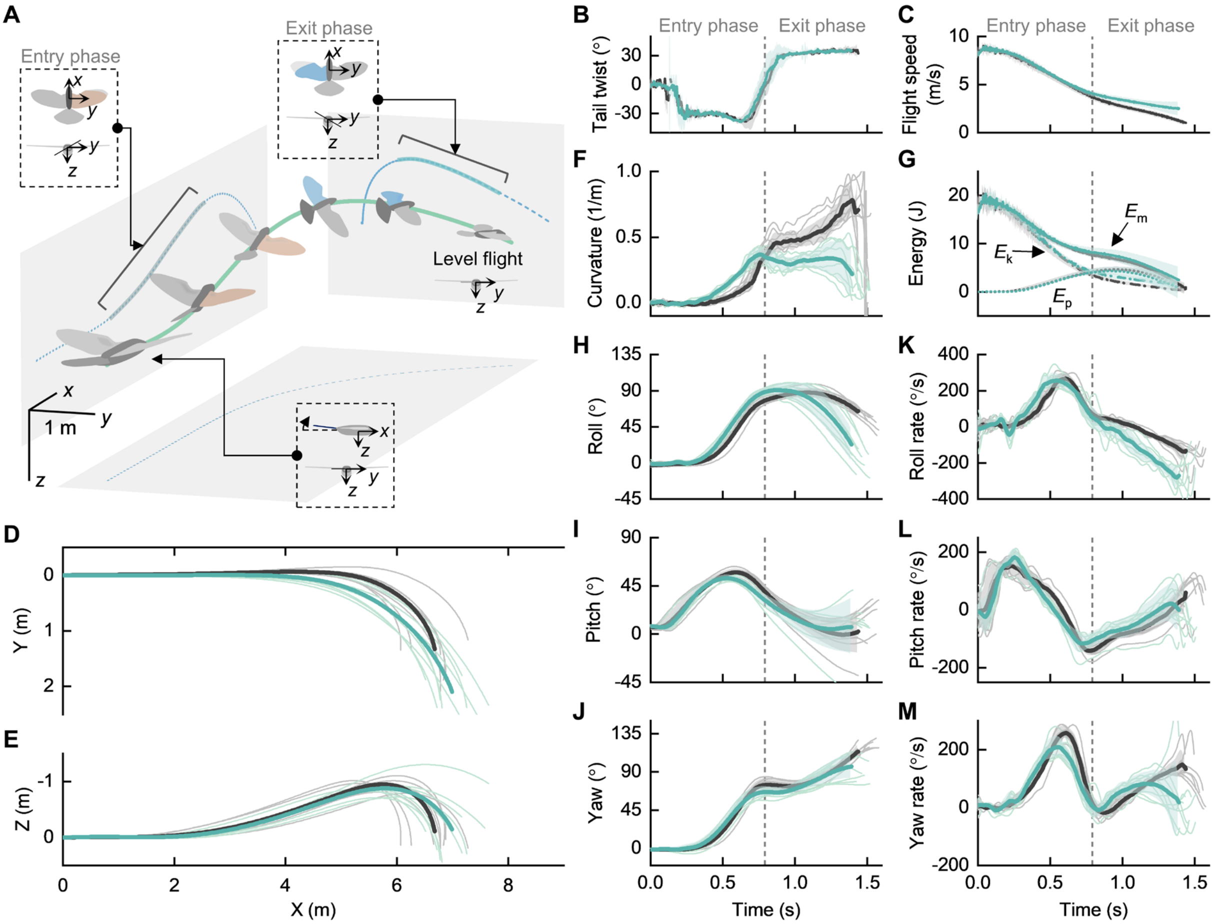

Fig. 4. High-speed sharp turning maneuvers enabled by tail twist with (green) and without (black) coordination of wing shape morphing. (**A**) Illustration of the control input sequence used to perform a sharp turn with tail twist and wing morphing coordination. For the right turn, the drone deflected the elevator upward to execute a rapid pitch-up maneuver. Thereafter, negative tail twist and right wing folding were synchronously applied to create roll and yaw motion. At the peak of the altitude, positive tail twist and left wing folding were applied to return to the level flight. (**B** and **C**) Tail twist angles (B) and flight speeds (C) during flights with ($n = 10$, green) and without ($n = 8$, black) coordination of wing shape morphing. (**D** and **E**) Flight trajectories in the *XY* plane (D) and the *XZ* plane (E). (**F**) Curvature of the turns. (**G**) Kinetic (E_k), potential (E_p), and mechanical ($E_m = E_k + E_p$) energies during the turn. (**H** to **J**) Body attitude angles: roll (H), pitch (I), and yaw (J). (**K** to **M**) Body rates: roll rate (K), pitch rate (L), and yaw rate (M). In (B) to (M), thin lines represent individual flight trials; thick lines and shaded areas are the mean and SD from the mean, respectively.

regulate, and end a turn. Simultaneously, reduced lift at the tail induces a nose-up motion that increases the wing angle of attack, thus generating more lift to compensate for the loss induced by the banking motion and thus help preserve the flight altitude. We suggest that, among other control methods (*1*, *4*, *7*, *12*, *14*), tail twisting may be the most efficient approach for controlling steady turning maneuvers in birds, because it requires activating only one group of tail muscles. Other methods that rely on asymmetric wing sweep morphing or wing twisting may generate more effective roll moment (fig. S7) but necessitate additional muscular controls to counteract adverse yaw (*1*, *12*, *14*).

Furthermore, we showed that sharp turns at high speed can leverage tail twisting in combination with a rapid pitch-up maneuver that not only substantially reduces flight speed but also enhances the effectiveness of roll moments generated by the tail twist (Fig. 2D). The results also showed that faster return to level flight after a turn can be achieved by coordinating tail twisting with asymmetric wing morphing, although the low flight speed at this stage may force birds to use powerful flaps to regain initial flight conditions.

Together, our findings with an avian-informed drone contribute to a better understanding of avian turning behaviors that are difficult to study with animals in controlled laboratory experiments. Although there are gaps in the morphological complexity and range of motion when compared with birds, the aerodynamic forces generated by the feathered drone are comparable with those of a hawk wing (fig. S2) (*53*, *54*). Last, the results described here have implications for effective control of drones with morphing aerial surfaces, thus broadening their range of applications across diverse environments, from open spaces to complex confined areas such as cities or dense forests.

MATERIALS AND METHODS

Feathered wing and tail design

Wing skeletal architecture

The mechanical wing skeletal structure was designed adapting morphological parameters of a hawk wing skeleton. It is composed of three segments (humerus-, ulna-, and manus-like linkages) made of a 1-mm glass fiber composite sheet that can rotate around the shoulder, elbow, and wrist joints (Fig. 5). The motion of the three segments is coupled through two pulley-string mechanisms, enabling the wing to be actuated by only one servomotor. The first pulley, with its radius r_1, is fixed to the body frame at the shoulder joint and connected to the second pulley with radius r_2, which is fixed to the ulna-like linkage at the elbow joint, through string 1. Simultaneously, the third pulley, with radius r_3 fixed to the humerus-like linkage and rotated around the elbow joint, is connected by string 2 to

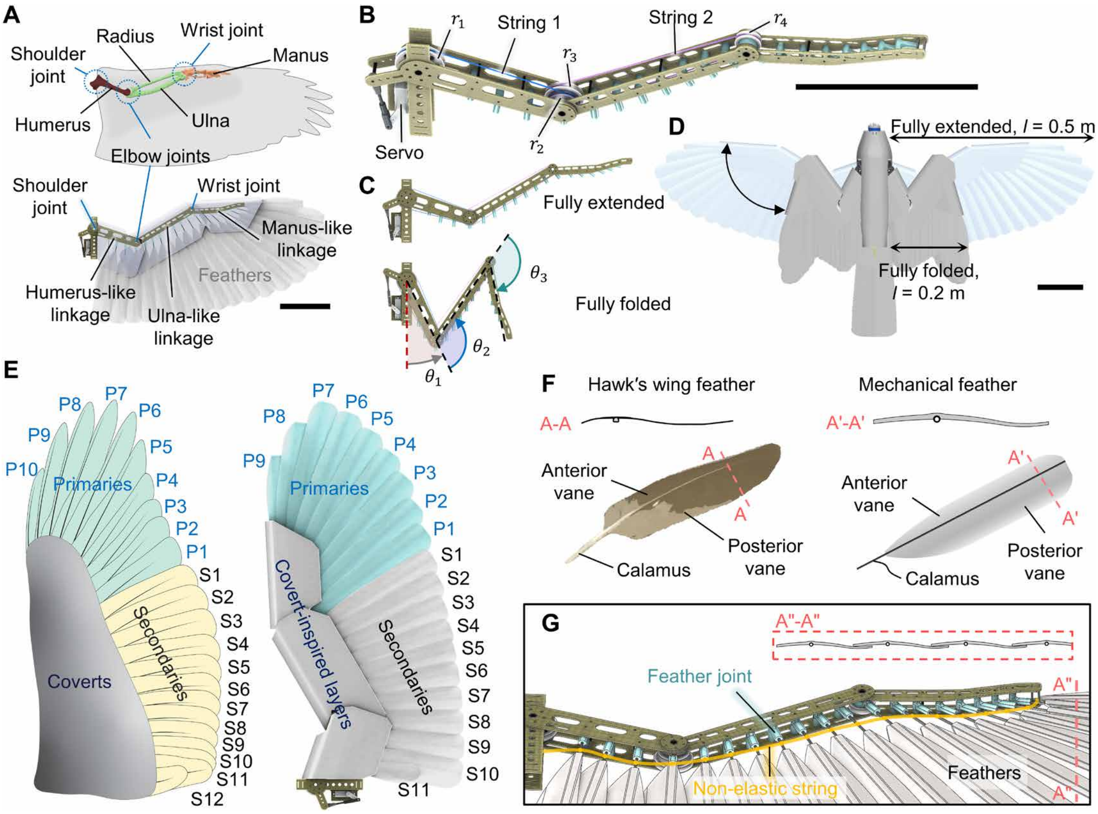

Fig. 5. Bioinformed wing skeletal and feather design. (**A**) Morphing wing design with multisegment, multijoint skeleton inspired by bird wing. Scale bar, 10 cm. (**B**) Detail of the wing skeleton driven by a single servomotor through two coupled pulley-string mechanisms. (**C**) Wing skeleton in fully extended and fully folded configurations. (**D**) The bird-inspired morphing wing enables the drone to change wingspan and surface area. Scale bar, 10 cm. (**E**) The wing is formed by primary-, secondary- and covert-inspired feathers, resembling those of a bird wing. (**F**) Feather design with a bird-inspired vane and calamus or quill. (**G**) The feathers are connected to the skeletal structure through in-plane rotating joints. The quills of the feathers are interconnected though a nonelastic tendon (yellow) to ensure that all the feathers still overlap consistently to form a complete surface during wing morphing.

the fourth pulley with radius r_4. This last pulley is affixed to the manus-like linkage and rotated around the wrist joint. Thus, range of motion of each segment can be determined by

$$\Delta\theta_3 = \frac{r_3}{r_4}\Delta\theta_2 = \frac{r_3 r_1}{r_4 r_2}\Delta\theta_1 \tag{1}$$

where θ_1, θ_2, and θ_3 are the sweeping angles of the humerus, ulna, and manus linkages, respectively (Fig. 5), and $\Delta\theta_i = |\theta_i^{\text{fully extended}} - \theta_i^{\text{fully folded}}|$, where $i = 1, 2,$ and 3.

Wing feathers

The wing was formed with 20 lightweight artificial feathers, including 9 primary (P1 to P9) and 11 secondary (S1 to S11) feathers, as shown in Fig. 5E. Inspired by a bird feather, the artificial feather was composed of a 1-mm S-shape vane made of flexible expanded polypropylene (EPP) foam with a density of 45 kg/m^3 and a reinforced calamus or quill made of a 1.5-mm carbon fiber tube. All feathers, except for the primary feather P9 that was fixed to the tip of the manus-like linkage, were attached to feather joints on the skeletal structure that could passively rotate in the wing plane (Fig. 5). The carbon shafts of the feathers are interconnected by a nonelastic tendon with one end attached to the body frame and the other end fixed to the manus-like linkage. Through this design, the 20 feathers form a configuration vector $\mathbf{q}$ with $\dim[\mathbf{q}] = 20$ and are underactuated via wing skeletal control with a single degree of freedom (*12*, *55*). The feathers' ranges of motion are also constrained to ensure that all the feathers still overlap consistently to form a complete surface when the wing is fully extended (Fig. 5G).

Wing covert

Birds overlay their wing skeletons by numerous overlapping covert feathers to streamline the wing. Replicating such coverts may cause mechanical complexity and increased wing mass. To replace the role of the coverts, we covered the mechanical wing skeletal structures and the feather shafts with discrete lightweight layers made of EPP foam (20 kg/m^3). The three covert-inspired layers overlap each other at the elbow and wrist joints to facilitate morphing (Fig. 5E).

Tail structure and feathers

The tail is capable of controlling independently four degrees of freedom, including shape morphing, twisting, elevator deflection, and lateral deflection, which was deactivated in this study (Fig. 6). It was formed by 11 overlapping feathers that distribute symmetrically across the body's symmetric plane (x-z plane). Except for the fixed central feather with symmetric anterior and posterior vanes, the other tail feathers, which have a similar shape to the wing feathers, could rotate on the tail plane around feather joints located at the tail skeletal structure made of a 0.5-mm glass fiber composite sheet. The feather shafts are interconnected by a prestretched three-dimensional (3D)–printed elastic tendon (NinjaFlex 85A). Similar to the previous design (*13*), we used a servomotor to actively and synchronously actuate the two outermost feathers through a nonelastic fishing cable (diameter of 0.4 mm, Spiderwire Dura-4 Braid, 45 kg) running through the center of the universal tail joint and along the inside of the hollow rectangular body shaft. The tail spread is thus activated by pulling the cable using the servomotor, whereas the elastic force of the tendon triggers the tail fold. Similar to the wing, the morphing tail is an underactuated system. The maximum tail spread

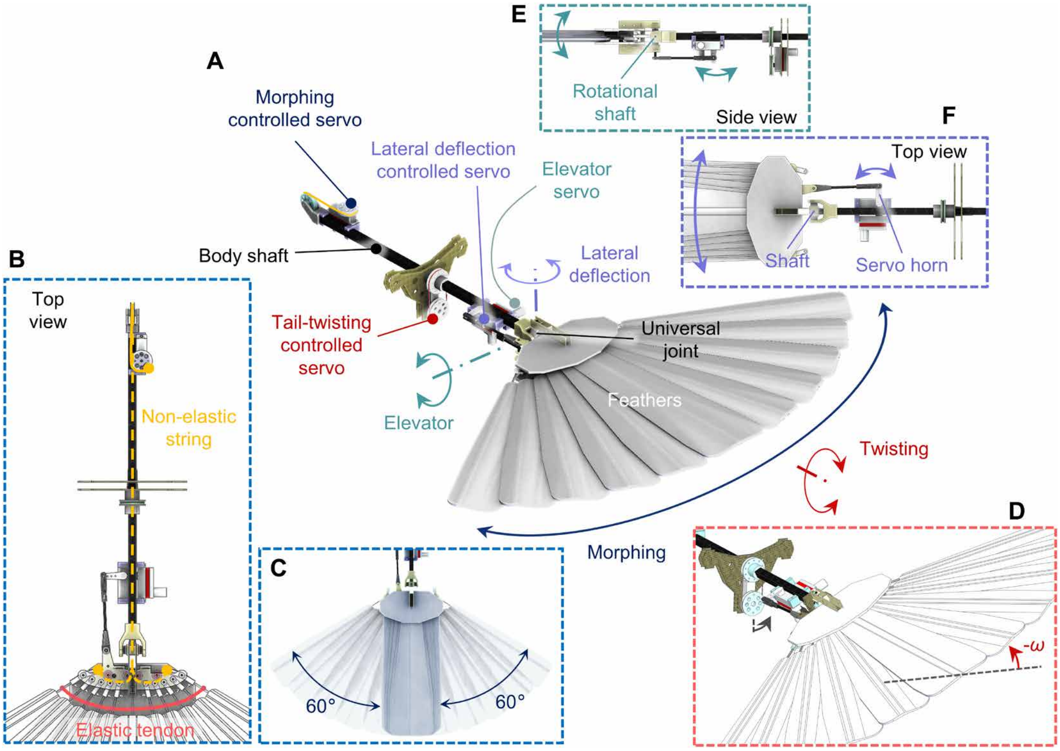

Fig. 6. Rudderless morphing tail design. (**A**) The tail formed by 11 overlapping feathers is capable of shape morphing, twisting, elevator deflection, and lateral deflection. (**B**) Top view of the tail shape morphing mechanism. (**C**) The tail in fully folded and fully spread configurations. (**D**) Mechanism of tail twisting. (**E**) Side view of the elevator-controlled mechanism. (**F**) Top view of the lateral deflection-controlled mechanism. This tail motion was locked in this study.

angle is 120°, which was estimated to provide optimal lift-to-drag ratio (*40*).

The tail could rotate around a universal joint that enables both elevator and lateral deflection controls (*13*), actuated by two servomotors affixed to the body shaft. To control tail twist, we split the body shaft into anterior and posterior parts. While the anterior part is fixed to the fuselage, the posterior part—where the tail is located—can rotate around it via a bearing (Fig. 6). By connecting this rotating shaft to a servomotor through a pulley-string mechanism, tail twist is fully actuated with a maximum twisting angle of ±60°.

Drone fabrication and avionics

We fabricated glass fiber composite sheets using a CO_2 laser cutter (Trotec Speedy 400) for the wing and tail skeletal structures and the supported frames that link the wing bases to the body shaft made of 6 mm–by–6 mm carbon fiber square tubes (fig. S1). All the pulleys, joints, and servomotor holders were 3D-printed in acrylonitrile butadiene styrene using a Stratasys Dimension Elite printer. The fabricated parts were then assembled manually and bonded together by cyanoacrylate super glue. We connected the pulleys located at the wing joints using 0.4-mm durable strings (Spiderwire Dura-4 Braid, 45 kg) to create the pulley-string mechanisms that drive the wing shape morphing. We fabricated the EPP foams for the feather vanes, coverts, and body cover using a hot wire machine (CNC-Multitool CUT 1620S). The feather vane was attached to the 1.5-mm carbon fiber quill using the foam adhesive (UHU Por). The quill was then inserted into the feather joint, which can rotate around a 1.5-mm carbon shaft in the skeletal structure.

To actuate the wing and tail morphing, we used KST X08plus V2 servomotors (KST digital servo, 5.3 kg·cm at 8.4V). For propulsion, we used a brushless dc motor (T-Motor AT-2306 KV2300), an 8 inch–by–4.5 inch (20.32 cm–by–11.43 cm) GWS propeller, a Pulsar A-15 speed controller, and a three-cell 900-mAh lithium polymer battery. An eight-channel FrSKY RX8R receiver was used to communicate with the pilot through the Taranis X9D Plus transmitter. The mass of the LisRaptor drone with a wingspan of 1.1 m and full body length of 0.54 m was 460 g.

Aerodynamic characterizations

Wind tunnel experiments

We characterized the aerodynamics of the feathered drone in a 2 m–by–1.75 m open wind tunnel (WindShape; turbulence intensity, <1%) made of an 8-by-7 array of controllable fan modules at the mean wind speed of 7 m/s, which is similar to the gliding speeds of hawks (*2*, *37*), corresponding to a Reynolds number of 85,101 for the drone. To acquire the aerodynamic forces and torques, we placed the drone on a calibrated six-axis force/torque sensor (ATI Nano 25, force resolution of 0.0625 N, torque resolution of 0.75 mNm) mounted at the extended tip of a robotic arm (TX-90, Stäubli) positioned in front of the wind tunnel. The robotic arm was programmable to systematically change the angle of attack of the drone from −8° to 36° at 4° steps. The force/torque sensor was located at the CG of the drone. The force/torque signals were logged by the NI-DAQmx 9.5.1 logger (National Instruments) through the installed ATI DAQ F/T software (ATI Industrial Automation) at a sampling rate of 3000 Hz with an averaging level of 5. At each angle of attack, we recorded the data for 8 s (4800 data points). Before starting the measurement, we zeroed all forces and torques at a 0° angle of attack and no-speed condition. For constant power input, we used an external dc power supply (PeakTech 6226) to power the servomotors for controlling different wing and tail morphing configurations. The propeller was removed during the measurement; therefore, the results exclude effects of propeller slipstream, considering similar flight conditions as in birds. We first validated lift and drag generation of the feathered drone by comparing them with those of a hawk wing within a similar range of Reynolds number (*53*). We then measured the forces and torques generated by various wing shape morphing both symmetrically and asymmetrically, tail shape morphing, and tail twisting.

We also conducted wind tunnel experiments to investigate the effect of rate of change in tail twist on the roll motion (fig. S6). We placed the LisRaptor drone on the extended tip of the robotic arm, which allows only one degree of freedom in roll. We then placed markers on the drone and used a motion tracking system (26 Optitrack cameras, 240 Hz) to monitor its roll motion in response to the tail twist input signals. The drone was commanded to twist its tail from 0° to −30° with step, 0.5-s, and 1.0-s slowdown input signals.

Data processing

The force/torque sensor can record three force (F_x, F_y, and F_z) and three torque (roll: M_x, pitch: M_y, and yaw: M_z) components in the *xyz* body coordinate system. By using the measured F_x and F_y, we calculated lift (L) and drag (D)

$$L = -\left(F_x - W\sin(\alpha)\right)\sin(\alpha) + \left(F_z - W(1-\cos(\alpha))\right)\cos(\alpha) \quad (2)$$

$$D = \left(F_x - W\sin(\alpha)\right)\cos(\alpha) + \left(F_z - W(1-\cos(\alpha))\right)\sin(\alpha) \quad (3)$$

where W is the weight of the drone used in the measurement and α denotes the angle of attack. The nondimensional lift coefficient (C_L) and drag coefficient (C_D) were then calculated as

$$C_L = \frac{2L}{\rho S_w V^2},\ C_D = \frac{2D}{\rho S_w V^2} \quad (4)$$

where ρ denotes the air density, S_w is the wing area of the fully extended configuration, and V is the input flow speed. Thereafter, we obtained pitch, roll, and yaw torques in coefficient form

$$C_m = \frac{2M_y}{\rho S_w \bar{c} V^2}, C_l = \frac{2M_x}{\rho S_w b V^2}, C_n = \frac{2M_z}{\rho S_w b V^2} \quad (5)$$

where $\bar{c}$ is the mean wing chord, b is the tip-to-tip wingspan, C_l is the roll coefficient, and C_n is the yaw coefficient.

Flow visualization

We used a Probe Capture with a hand-guided five-hole pressure probe for real-time visualization and measurement of the airflow field (*56*). We fixed the LisRaptor on the extended tip of the robotic arm at an angle of attack of 16°, positioned in front of the wind tunnel with an inflow speed of 7 m/s. We defined a visualization plane (0.7 m by 0.5 m) perpendicular to the airflow direction and located at the middle chord of the tail. The instantaneous position of the probe, tracked by a motion tracking system (26 Optitrack cameras) at a tracking frequency of 240 Hz, was synchronized with the inflow data streamed from the probe. We conducted measurements for the fully extended tail at a twisting angle of −30° with and without the presence of the wings. The measured data were postprocessed in open-source multiplatform software (ParaView 5.11.1) for data analysis and visualization.

Flight experiments

Flight experiments were conducted in a 10 m–by–10 m–by–8 m indoor flight arena equipped with a safety net and a motion tracking system (26 Optitrack cameras, 240 Hz) that can track the reflective markers located on the drone (fig. S4). We launched the LisRaptor drone using a custom-built, programmable linear launcher at speeds of approximately 7 m/s for steady turns and 9 m/s for sharp aerobatic turns. We performed experiments on both the feathered and fixed-wing drones with similar morphologies that are capable of tail twisting. We defined a fixed XYZ coordinate system located at the tip of the launcher, in which the XY plane is the horizontal plane and the Z axis points downward. We first trimmed the drones to maintain a straight flight path and similar body attitudes without any control inputs (Fig. 3, B to L, black). We set the throttle at 50% to maintain a consistent flight speed of about 7 m/s of the drone after release from the launcher. We set the tail-twist angle to $\omega = \pm 30°$ in all experiments because it generated the highest rolling moment among tested angles (Fig. 2D).

To test the open-loop response of the drone to tail twist under a steady turn scenario, we automated flight trials for repeatability by predetermining tail-twist control inputs while locking other control surfaces. In experiments with single-phase tail twist (Fig. 3, B to L, red), the tail remained locked at a twist angle of −30° throughout flight. In experiments with two-phase tail twist (Fig. 3, B to L, blue), the flights were initiated with the tail-twist angle set at $\omega = -30°$ until the drone reached a banked angle (ϕ) of approximately 20°, where the flight speed began to decrease as observed in the single-phase tail twist experiments in Fig. 3C. Thereafter, the tail was switched to the twist angle of 30° to recover the level flight at the setting time $t_{\omega\rightarrow 30°} = t_0 + t_{\phi=20°} - 0.5\Delta t_{\omega,-30°\rightarrow 30°}$, where t_0 is the launching time, $t_{\phi=20°}$ denotes the time needed to reach the banked angle of 20° obtained in the tests of single-phase tail twist, and $\Delta t_{\omega,-30°\rightarrow 30°}$ represents the time spent to twist the tail from −30° to 30° in response to a step input signal (fig. S6B).

For sharp right turns, we conducted experiments with three sets of coordinated configurations. In all experiments, we launched the drone with an upward tail deflection of $\delta_p = -10°$ (*13*) from the beginning to execute the pitch-up maneuver immediately after release from the launcher. We first conducted experiments with configuration I, which consists of tail upward deflection and twist. From the motion tracking system, we could determine the attitude of the drone during the pitch-up maneuver. We assumed that the angle of attack was similar to the pitch angle at this initial stage ($\theta \approx \alpha$). When the pitch angle (θ) reached about 20° at the time $t_{\theta=20°}$, a negative tail twist of −30° was applied ($t_{\omega\rightarrow -30°} = t_{\theta=20°}$) to roll and yaw the drone to the right. Note that, to ensure a desired flight turn, the tail twist should be activated after the drone reaches a pitch angle that is larger than the tail deflection angle $\left(\theta > |\delta_p|\right)$. Otherwise, adverse yaw may occur, impairing turning performance. Therefore, we triggered the tail twist at $\theta = 20°$ because the tail angle of attack (α_t) is close to $\left(\theta - |\delta_p|\right) = 10°$, where the roll moment starts developing (Fig. 2D). With that upward deflection and twist of the tail, the drone reached peak altitude at the time t_{peak}, whereas the roll angle approached the set limit of 90° (Fig. 4, H to J, black). We then reversed the tail twist to 30° at $t_{\omega\rightarrow 30°} = t_{\text{peak}}$ to generate a counteracting roll moment and return to the level flight. In flight tests using configuration II (tail upward deflection, tail twist, and asymmetric wing shape morphing), we triggered the wing tucking and tail twisting simultaneously ($t_{\text{tuck,right wing}} = t_{\omega\rightarrow -30°}$ and $t_{\text{tuck,left wing}} = t_{\omega\rightarrow 30°}$). In flight tests using configuration III (tail upward deflection and asymmetric wing shape morphing but no tail twist; fig. S9), only the right wing tucking was applied and triggered at the same time of negative tail twisting used in configurations I and II. For consistency, the flight test in each set of coordinated configurations was repeated at least seven times.

From the measured flight data extracted by the motion tracking system, we calculated the curvature (κ) and radius (r) of the horizontal turn (*57*)

$$\kappa = \frac{\frac{d^2Y}{dX^2}}{\sqrt{\left(1+\left(\frac{dY}{dX}\right)^2\right)^3}},\quad r = \frac{1}{\kappa} \tag{6}$$

Last, we obtained mechanical (E_m), kinetic (E_k), and potential (E_p) energies from the following equation

$$E_\text{m} = E_\text{k} + E_\text{p} = \frac{1}{2}m|V|^2 + mg\left(Z - Z_0\right) \tag{7}$$

where $|V| = \sqrt{\dot{X}^2 + \dot{Y}^2 + \dot{Z}^2}$ is the flight speed (meters per second) and m is the mass of the drone (kilograms).

Statistical analysis

We used mean values (±SD) to represent aerodynamic force and torque data in Figs. 1 (K and L) and 2 (A to E) and figs. S3 and S7; velocity data in Fig. 2 (H and I); flight data in Figs. 3 (B to L) and Fig. 4 (B to M) and figs. S8 and S9; and roll angle data in fig. S6 (B to D). We obtained the aerodynamic data from the force/torque sensor over a 4-s period, which generated 2400 data points at each angle of attack, excluding those during the transition stage between angles. For other data, we conducted the experiments n times, as reported in the figures.

Supplementary Materials

The PDF file includes:

Figs. S1 to S9
Table S1

Other Supplementary Material for this manuscript includes the following:

Movies S1 to S6

REFERENCES AND NOTES

1. D. R. Warrick, M. W. Bundle, K. P. Dial, Bird maneuvering flight: Blurred bodies, clear heads. *Integr. Comp. Biol.* **42**, 141–148 (2002).
2. J. A. Cheney, J. P. J. Stevenson, N. E. Durston, M. Maeda, J. Song, D. A. Megson-Smith, S. P. Windsor, J. R. Usherwood, R. J. Bomphrey, Raptor wing morphing with flight speed. *J. R. Soc. Interface* **18**, 20210349 (2021).
3. J. A. Gillies, A. L. R. Thomas, G. K. Taylor, Soaring and manoeuvring flight of a steppe eagle *Aquila nipalensis*. *J. Avian Biol.* **42**, 377–386 (2011).
4. D. Lentink, U. K. Müller, E. J. Stamhuis, R. de Kat, W. van Gestel, L. L. M. Veldhuis, P. Henningsson, A. Hedenström, J. J. Videler, J. L. van Leeuwen, How swifts control their glide performance with morphing wings. *Nature* **446**, 1082–1085 (2007).
5. C. Harvey, V. B. Baliga, J. C. M. Wong, D. L. Altshuler, D. J. Inman, Birds can transition between stable and unstable states via wing morphing. *Nature* **603**, 648–653 (2022).
6. S. Barbarino, O. Bilgen, R. M. Ajaj, M. I. Friswell, D. J. Inman, A review of morphing aircraft. *J. Intel. Mater. Syst. Struct.* **22**, 823–877 (2011).
7. C. Harvey, L. L. Gamble, C. R. Bolander, D. F. Hunsaker, J. J. Joo, D. J. Inman, A review of avian-inspired morphing for UAV flight control. *Prog. Aerospace Sci.* **132**, 100825 (2022).
8. C. Harvey, G. de Croon, G. K. Taylor, R. J. Bomphrey, Lessons from natural flight for aviation: Then, now and tomorrow. *J. Exp. Biol.* **226**, jeb245409 (2023).

9. M. Abdulrahim, R. Lind, "Flight testing and response characteristics of a variable gull-wing morphing aircraft," paper presented at AIAA Guidance, Navigation, and Control Conference and Exhibit, Providence, RI, USA, 16 to 19 August 2004.
10. D. T. Grant, M. Abdulrahim, R. Lind, Flight dynamics of a morphing aircraft utilizing independent multiple-joint wing sweep. *Int. J. Micro Air Vehicles* **2**, 91–106 (2010).
11. M. Di Luca, S. Mintchev, G. Heitz, F. Noca, D. Floreano, Bioinspired morphing wings for extended flight envelope and roll control of small drones. *Interf. Focus*, **7**, 20160092 (2017).
12. E. Chang, L. Y. Matloff, A. K. Stowers, D. Lentink, Soft biohybrid morphing wings with feathers underactuated by wrist and finger motion. *Sci. Robot.* **5**, eaay1246 (2020).
13. E. Ajanic, M. Feroskhan, S. Mintchev, F. Noca, D. Floreano, Bioinspired wing and tail morphing extends drone flight capabilities. *Sci. Robot.* **5**, eabc2897 (2020).
14. E. Ajanic, M. Feroskhan, V. Wüest, D. Floreano, Sharp turning maneuvers with avian-inspired wing and tail morphing. *Commun. Eng.* **1**, 34 (2022).
15. Y. Liu, J. Zhang, L. Gao, Y. Zhu, B. Liu, X. Zang, H. Cai, J. Zhao, Employing wing morphing to cooperate aileron deflection improves the rolling agility of drones. *Adv. Intel. Syst.* **5**, 2300420 (2023).
16. S. L. Jeger, V. Wüest, C. Toumieh, D. Floreano, Adaptive morphing of wing and tail for stable, resilient, and energy-efficient flight of avian-informed drones. arXiv:2403.08598 [cs.RO] (2024).
17. A. L. R. Thomas, On the tails of birds. *BioScience*, **47**, 215–225 (1997).
18. H. Oehme, Die flugsteuerung des vogels. III. Flugmanoever de karnweihe (*Circus cyaneus*). *Beitr. Vogelkunde* **22**, 73–82 (1976).
19. R. G. Hoey, Exploring bird aerodynamics using radio-controlled models. *Bioinspir. Biomim.* **5**, 045008 (2010).
20. J. R. Parga, M. F. Reeder, T. Leveron, K. Blackburn, Experimental study of a micro air vehicle with a rotatable tail. *J. Aircraft* **44**, 1761–1768 (2007).
21. J. Katz, Lateral aerodynamics of delta wings with leading-edge separation. *AIAA Journal*, **22**, 323–328 (1984).
22. J. Katz, A. Plotkin, *Low Speed Aerodynamics: From Wing Theory to Panel Methods* (Cambridge Univ. Press, ed. 2, 2001).
23. A. L. R. Thomas, On the aerodynamics of birds' tails. *Philos. Trans. R. Soc. London Ser B Biol. Sci.* **340**, 361–380 (1993).
24. W. J. Maybury, J. M. V. Rayner, L. B. Couldrick, Lift generation by the avian tail. *Proc. Biol. Sci.* **268**, 1443–1448 (2001).
25. M. R. Evans, Birds' tails do act like delta wings but delta-wing theory does not always predict the forces they generate. *Proc. Biol. Sci.* **270**, 1379–1385 (2003).
26. D. Hummel, "On the aerodynamics of the tail in birds" in *Acta XX Congressus Internationalis Ornithologici* (Ornithological Congress Trust Board, 1990), pp. 730–747.
27. E. L. Corvidae, R. O. Bierregaard, S. E. Peters, Comparison of wing morphology in three birds of prey: Correlations with differences in flight behavior. *J. Morphol.* **267**, 612–622 (2006).
28. J. J. Videler, *Avian Flight* (Oxford Univ. Press, 2006).
29. R. J. Vazquez, The automating skeletal and muscular mechanisms of the avian wing (Aves). *Zoomorphology* **114**, 59–71 (1994).
30. A. K. Stowers, L. Y. Matloff, D. Lentink, How pigeons couple three-dimensional elbow and wrist motion to morph their wings. *J. R. Soc. Interface* **14**, 20170224 (2017).
31. L. Y. Matloff, E. Chang, T. J. Feo, L. Jeffries, A. K. Stowers, C. Thomson, D. Lentink, How flight feathers stick together to form a continuous morphing wing. *Science* **367**, 293–297 (2020).
32. S. Gudmundsson, *General Aviation Aircraft Design: Applied Methods and Procedures* (Butterworth-Heinemann, 2013).
33. A. L. R. Thomas, The aerodynamic costs of asymmetry in the wings and tail of birds: Asymmetric birds can't fly round tight corners. *Proc. R. Soc. London Ser. B Biol. Sci.* **254**, 181–189 (1993).
34. J. R. Usherwood, J. A. Cheney, J. Song, S. P. Windsor, J. P. J. Stevenson, U. Dierksheide, A. Nila, R. J. Bomphrey, High aerodynamic lift from the tail reduces drag in gliding raptors. *J. Exp. Biol.* **223**, jeb214809 (2020).
35. W. J. Maybury, J. M. V. Rayner, The avian tail reduces body parasite drag by controlling flow separation and vortex shedding. *Proc. R. Soc. London Ser. B Biol. Sci.* **268**, 1405–1410 (2001).
36. J. Song, J. A. Cheney, R. J. Bomphrey, J. R. Usherwood, Virtual manipulation of tail postures of a gliding barn owl (*Tyto alba*) demonstrates drag minimization when gliding. *J. R. Soc. Interface* **19**, 20210710 (2022).
37. V. A. Tucker, Pitching equilibrium, wing span and tail span in a gliding Harris' hawk, *Parabuteo unicinctus*. *J. Exp. Biol.* **165**, 21–41 (1992).
38. F. W. Headley, Birds' methods of steering. *Nature* **48**, 293–294 (1893).
39. G. Sachs, Tail effects on yaw stability in birds. *J. Theor. Biol.* **249**, 464–472 (2007).
40. A. L. R. Thomas, A. Balmford, How natural selection shapes birds' tails. *Am. Nat.* **146**, 848–868 (1995).
41. J. M. Hull, A. C. Hull, B. N. Sacks, J. P. Smith, H. B. Ernest, Landscape characteristics influence morphological and genetic differentiation in a widespread raptor (*Buteo jamaicensis*). *Mol. Ecol.* **17**, 810–824 (2008).
42. A. L. R. Thomas, G. K. Taylor, Animal flight dynamics I. Stability in gliding flight. *J. Theor. Biol.* **212**, 399–424 (2001).
43. D. R. Warrick, K. P. Dial, A. A. Biewener, Asymmetrical force production in the maneuvering flight of pigeons. *Auk* **115**, 916–928 (1998).
44. D. R. Warrick, K. P. Dial, Kinematic, aerodynamic and anatomical mechanisms in the slow, maneuvering flight of pigeons. *J. Exp. Biol.* **201**, 655–672 (1998).
45. I. G. Ros, L. C. Bassman, M. A. Badger, A. N. Pierson, A. A. Biewener, Pigeons steer like helicopters and generate down- and upstroke lift during low speed turns. *Proc. Natl. Acad. Sci. U.S.A.* **108**, 19990–19995 (2011).
46. T. L. Hedrick, A. A. Biewener, Low speed maneuvering flight of the rose-breasted cockatoo (*Eolophus roseicapillus*). I. Kinematic and neuromuscular control of turning. *J. Exp. Biol.* **210**, 1897–1911 (2007).
47. J. M. V. Rayner, Bounding and undulating flight in birds. *J. Theor. Biol.* **117**, 47–77 (1985).
48. J. M. V. Rayner, P. W. Viscardi, S. Ward, J. R. Speakman, Aerodynamics and energetics of intermittent flight in birds. *Am. Zool.* **41**, 188–204 (2001).
49. M. KleinHeerenbrink, L. A. France, C. H. Brighton, G. K. Taylor, Optimization of avian perching manoeuvres. *Nature* **607**, 91–96 (2022).
50. B. Ponitz, A. Schmitz, D. Fischer, H. Bleckmann, C. Brücker, Diving-flight aerodynamics of a peregrine falcon (*Falco peregrinus*). *PLOS ONE* **9**, e86506 (2014).
51. V. A. Tucker, Gliding flight: Speed and acceleration of ideal falcons during diving and pull out. *J. Exp. Biol.* **201**, 403–414 (1998).
52. A. C. Carruthers, A. L. R. Thomas, S. M. Walker, G. K. Taylor, Mechanics and aerodynamics of perching manoeuvres in a large bird of prey. *Aeronaut. J.* **114**, 673–680 (2010).
53. P. C. Withers, An aerodynamic analysis of bird wings as fixed aerofoils. *J. Exp. Biol.* **90**, 143–162 (1981).
54. C. Harvey, D. J. Inman, Aerodynamic efficiency of gliding birds vs comparable UAVs: A review. *Bioinspir. Biomim.* **16**, 031001 (2021).
55. R. Tedrake, Underactuated robotics: Learning, planning, and control for efficient and agile machines course notes for MIT 6.832 (2009).
56. J. Bartl, A. Müller, A. Landolt, F. Mühle, M. Vatn, L. Oggiano, L. Sætran, Validation of the real-time-response ProCap measurement system for full field wake scans behind a yawed model-scale wind turbine. *J. Phys. Conf. Ser.* **1104**, 012018 (2018).
57. J. D. Lawrence, *A Catalog of Special Plane Curves* (Courier Corporation, 2013).

Acknowledgments: We thank E. Ajanic for comments on the drone design and previous work on the LisHawk drone and V. Wüest, S. Jeger, M. Askari, and R. Zufferey for designing and building the drone launcher. **Funding:** This project was partially funded by the European Union's Horizon 2020 research and innovation programme under grant agreement ID: 871479 AERIAL-CORE and by Armasuisse grant no. 8003529756. **Author contributions:** H.-V.P. conceived the idea and designed the research, built the robot, performed all experiments, processed and analyzed the data, and wrote the manuscript. D.F initiated the project and contributed to the research design, data analysis, and writing of the manuscript. Both authors gave final approval for publication. **Competing interests:** The authors declare that they have no competing interests. **Data and materials availability:** All data needed to support the conclusions of this manuscript are included in the main text or the Supplementary Materials. The data for this study have been deposited in the public repository at https://doi.org/10.6084/m9.figshare.25809412.

Submitted 30 January 2024
Accepted 21 October 2024
Published 20 November 2024
10.1126/scirobotics.ado3890

Science Robotics

A twist of the tail in turning maneuvers of bird-inspired drones

Hoang-Vu Phan and Dario Floreano

Sci. Robot. **9** (96), eado3890. DOI: 10.1126/scirobotics.ado3890

Editor's summary

During banked turns while soaring, raptors have been observed twisting their tails without moving their wings to compensate for adverse yaw. To better understand this phenomenon, Phan and Floreano designed a raptor-inspired feathered drone with morphing wings and twisting tail. The drone, named LisRaptor, features a bioinformed skeleton frame with feather-like foam structures, wings that can morph to different wing spans, and a tail capable of twisting around the body axis. Experiments performed in an indoor wind tunnel revealed that tail twisting generated aerodynamic control forces to initiate both low-speed steady banked turns and high-speed sharp turns. —Melisa Yashinski

Science Robotics (ISSN 2470-9476) is published by the American Association for the Advancement of Science. 1200 New York Avenue NW, Washington, DC 20005. The title *Science Robotics* is a registered trademark of AAAS.